Title

A quantitative CBCT pipeline based on 2D antiscatter grid and grid-based scatter sampling for image-guided radiation therapy.

Journal

Medical Physics, 50(12)

Authors

Bayat, Farhang
Ruan, Dan
Miften, Moyed
et al.

Publication Date

2023-12-01

DOI

10.1002/mp.16681

Peer reviewed

HHS Public Access

Author manuscript

Med Phys. Author manuscript; available in PMC 2024 December 01.

Published in final edited form as:

Med Phys. 2023 December ; 50(12): 7980–7995. doi:10.1002/mp.16681.

A quantitative CBCT pipeline based on 2D antiscatter grid and grid-based scatter sampling for image guided radiation therapy

Farhang Bayat[a], **Dan Ruan**[b], **Moyed Miften**[a], **Cem Altunbas**[a]

[a]Department of Radiation Oncology, University of Colorado School of Medicine, Aurora, CO 80045, USA.

[b]Department of Radiation Oncology, University of California Los Angeles, Los Angeles, CA 90095, USA.

Abstract

Background: Quantitative accuracy is critical for expanding the role of cone beam CT (CBCT) imaging from target localization to quantitative treatment monitoring and plan adaptations in radiation therapy. Despite advances in CBCT image quality improvement methods, quantitative accuracy gap between CBCT and multi-detector CT (MDCT) remains.

Purpose: In this work, a physics-driven approach was investigated that combined robust scatter rejection, raw data correction and iterative image reconstruction to further improve CBCT image quality and quantitative accuracy, referred to as quantitative CBCT (qCBCT).

Methods: qCBCT approach includes tungsten 2D antiscatter grid hardware, residual scatter correction with grid-based scatter sampling, image lag, and beam hardening correction for offset detector geometry linac-mounted CBCT. Images were reconstructed with iterative image reconstruction to reduce image noise. qCBCT was evaluated using a variety of phantoms to investigate the effect of object size and its composition on image quality, and image quality was benchmarked against clinical CBCT and gold standard MDCT images used for treatment planning.

Results: qCBCT provided statistically significant improvement in CT number accuracy and reduced image artifacts when compared to clinical CBCT images. When compared to gold standard MDCT, mean HU errors in qCBCT and clinical CBCT were 17±9 HU and 38±29 HU, respectively. Magnitude of phantom size dependent HU variations were comparable between MDCT and qCBCT images. With iterative reconstruction, contrast-to-noise ratio improved by 25% when compared to clinical CBCT protocols.

Conclusions: Combination of novel scatter suppression techniques and other data correction methods in qCBCT provided CT number accuracy comparable to gold standard MDCT used for treatment planning. This approach may potentially improve CBCT's promise in fulfilling the tasks

Corresponding Authors: Farhang Bayat, farhang.bayat@cuanschutz.edu, Postal Address: 1665 Aurora Court, Suite 1032 | MS F-706 | Aurora, CO 80045, Cem Altunbas, cem.altunbas@cuanschutz.edu, Postal Address: 1665 Aurora Court, Suite 1032 | MS F-706 | Aurora, CO 80045.

Conflict of Interest Statement

The authors have no conflicts to disclose.

that demand high quantitative accuracy, such as online dose calculations and treatment response assessment, in image guided radiation therapy.

Keywords

Cone beam computed tomography (CBCT); IGRT; quantitative imaging; adaptive radiation therapy

1. Introduction

Even though CBCT imaging is the most used 3D in-room imaging modality to localize targets during image guided radiation therapy (IGRT), its poor quantitative accuracy and tissue visualization remain a challenge in implementation of contemporary treatment paradigms, such as CBCT-based dose delivery monitoring and radiation treatment plan adaptations[1]. However, such approaches require accurate CT numbers and clear visualization of image features, which remain as challenges due to relatively poor image quality of CBCT images[2–4].

Reasons behind poor CBCT image quality are numerous, such as scattered radiation, motion artifacts due to long scan times, limitations of flat panel detectors (poor quantum efficiency, image lag, limited dynamic range), suboptimal image reconstruction due to circular source trajectory, and suboptimal beam hardening correction[5]. Cumulative effect of these problems yields poor CT number accuracy, increased noise, blurring, and lower contrast the collective effect of whom degrades visualization of anatomical structures and targets.

Among these, scattered radiation is considered one of the most fundamental problems in CBCT, for which we previously proposed and investigated a novel 2D antiscatter grid-based approach to address the issue[6–8]. While this approach can robustly suppress scatter[6,7,9], scatter suppression by itself is not sufficient to improve CBCT image quality to levels comparable to MDCT. Other data correction methods, such as image lag and beam hardening corrections, are needed. Furthermore, scatter correction along with relatively lower quantum efficiency and higher electronic noise of amorphous silicon flat panel detectors results in increased image noise in CBCT images[6,10,11]. If data correction and image denoising methods were to be combined with 2D antiscatter grid-based scatter suppression in one data processing pipeline, both HU accuracy and soft tissue visualization in CBCT imaging can be potentially improved further.

In this work, we developed a raw data processing and iterative reconstruction pipeline that is used in conjunction with a 2D antiscatter grid for high fidelity CBCT imaging in radiation therapy. The pipeline consists of a 2D antiscatter grid prototype[8,12], a measurement-based scatter correction method[6,13], image lag correction, and beam hardening correction. In addition, an iterative image reconstruction method was incorporated as part of the pipeline to reduce image noise. This approach is referred to as quantitative CBCT, or qCBCT.

Image quality improvement methods in CBCT have been extensively studied[5], and state-of-the-art clinical CBCT systems combine numerous image quality improvement methods in one data processing pipeline[14–19]. However, none of the existing work utilizes 2D antiscatter

grid-based scatter suppression in conjunction with software-based data correction and image denoising methods.

In short, the novelty of this work lies in the integration of 2D antiscatter grid-based scatter rejection and correction methods with existing raw data correction and iterative image reconstruction in one data processing pipeline, aimed towards CBCT-guided radiation therapy. This approach aims to close the gap in CT number accuracy between CBCT and MDCT for radiation therapy. In addition, this work benchmarks the image quality performance of our proposed approach for the first time with respect to state-of-the-art CBCT imaging methods used in C-shaped linacs and gold standard MDCT images in a comprehensive set of phantom experiments.

2. Method

2.1. Overview of data processing steps and image reconstruction

Overall flow of our data processing pipeline (Fig. 1) is explained in the following sections. Briefly, a CBCT scan was acquired with a 2D antiscatter grid in place, and by using a linac mounted CBCT system. CBCT projections were dark and flat field-corrected by the clinical CBCT system and subsequently exported for downstream processing, which are referred as raw projections.

Each raw projection was corrected for image lag, residual scatter, grid septal shadows (referred as gain correction), and beam hardening. For objects larger than transverse field of view, a truncation correction was also applied[20]. CBCT images were reconstructed either by using filtered backprojection or OS-ASD-POCS[21 22]. For filtered backprojection, an offset detector weighting scheme was implemented to reconstruct in offset detector geometry[23].

2.2. Image Lag Correction

Each CBCT projection inherits a residual signal from prior projections in a CBCT scan, known as image lag[24]. For image lag correction[25], a flood CBCT scan without 2D grid was acquired, and a second order exponential model was fitted to parameterize the mean signal intensity as a function of projection number in the scan, $I_{flood}^{fitted}(i), \quad i = 1\ldots, M$. Relative intensity difference between two consecutive flood projections yielded the relative image lag, referred as lag coefficient,

$$coeff_{flood}^{lag}(i) = \frac{I_{flood}^{fitted}(i+1) - I_{flood}^{fitted}(i)}{I_{flood}^{fitted}(i+1)}, \quad i = 1\ldots, M-1 \tag{1}$$

Subsequently, flood and phantom CBCT projections were corrected using the following,

$$Proj_{corrected}(i) = Proj_{uncorrected}(i) - Proj_{uncorrected}(i-1) \times coeff_{flood}^{lag}(1) - Proj_{uncorrected}(i-2) \times coeff_{flood}^{lag}(2) - \ldots - Proj_{uncorrected}(i-k) \times coeff_{flood}^{lag}(k), \quad k = \min(i-1, M) \tag{2}$$

where $Proj_{uncorrected}(i-k) \times coeff_{flood}^{lag}(k)$ represents the lag carried over from the frame $i-k$ to i. Since magnitude of image lag from one projection to subsequent projections goes down exponentially, only image lag up to M prior projections were accounted. $M = 300$ was used based on the visual evaluations of image lag correction (Fig. 2). This correction was applied consistently for both phantom and flood projections.

There are other potentially more robust lag correction techniques that model image lag after termination of the X-ray beam[26]. Such methods require the X-ray beam to be turned off and read out frames to measure lag, which cannot be achieved with the clinical system's current acquisition scheme. Therefore, they were not implemented in this pipeline.

2.3. Grid-Based Scatter Sampling (GSS) Method

While 2D grid rejects majority of scatter fluence, it does not fully eliminate scatter. To correct residual scatter, previously developed Grid-based Scatter Sampling method was employed[6,13]. For completeness, a brief description is provided. In the GSS method, a 2D antiscatter grid is employed as a residual scatter measurement, or "sampling", device. The grid's footprint, or septal shadow, acts as a micro-fluence modulator, where ratio of signal in grid holes to shadows in a small neighborhood of pixels varies as a function of scatter intensity. In gain-corrected projections, this variation in signal ratio manifests itself as a signal intensity difference, d, between pixels residing in grid shadows and adjacent pixels residing in grid holes. Assuming scatter intensity S is piecewise uniform in pixels residing both in grid shadows and grid holes in a small neighborhood of pixels (typically a 7×7 pixel region, corresponding to an area of 2.7×2.7 mm^2), scatter can be defined as[6,13],

$$S(x_1, y_1) = \frac{d(x_1, y_1)}{GM_{grid}(x_1, y_1) - GM_{hole}(x_2, y_2)} \tag{3}$$

Where x_1 and y_1 are for pixels in grid shadows and x_2 and y_2 are for pixels in grid holes. GM_{grid} and GM_{hole} are the values of gain maps (defined in 2.4) in grid septal shadows and holes, respectively.

Using Eq. 3, residual scatter was first estimated in pixels residing in grid shadows and subsequently, residual scatter values in each detector pixel were obtained via interpolation. Residual scatter was subtracted from projections to achieve scatter corrected projections.

2.4. Gain Correction

Gain or flat field correction procedure suppresses the 2D grid's septal shadows in projections and reduces grid-induced artifacts in CBCT images. A flood CBCT scan, i.e., a scan without a phantom, was acquired to characterize grid shadows in projections as a function of source or gantry angle[27]. Gain maps are generated as below:

$$GM(x, y, \varphi) = \frac{I_0}{Flood\ projections(x, y, \varphi)} \tag{4}$$

Where x and y are detector pixel indices and φ represents projection index (scan angle). Subsequently, gain maps are multiplied with CBCT projections at matching source angles.

2.5 Beam Hardening Correction

For polyenergetic x-rays, the log attenuation of projections can be calculated by

$$p = -\log\left(\frac{I}{I_0}\right) = -\log\left(\int \Omega(E) e^{-\int \mu_{E,s} ds} dE\right) \tag{5}$$

Where $\Omega(E)$ is the incident x-ray spectrum, I_0 and I represent the incident and transmitted intensities and $\mu_{E,s}$ is the linear attenuation coefficient of the object at a specific energy E and path s. The relationship between p and the path s is not linear, a problem known as beam hardening. In the clinical CBCT system, beam hardening is caused by both the imaged object and the aluminum bow tie filter[28]. To address this issue, a water-equivalent beam hardening correction method was implemented[28]. Mapping functions were generated for source spectra at 125 kVp and 140 kVp with 0.89 mm Titanium filtration[29,30], such that the projection log attenuation values have a linear relationship with water equivalent thickness of the object (path length). For any water equivalent path length s with bowtie thickness l a correction factor $CF(s,l)$ was calculated and log attenuation was updated:

$$p^*(s,l) = p(s,l) \times CF(s,l) \tag{6}$$

Methods that account for both water and bone beam hardening were not utilized in this study since such methods[31] require differentiation of bone and soft tissue regions in 3D images, which may be unreliable in the presence of anatomical motion and the slowly rotating linac gantry.

2.6. Iterative Reconstruction

To reduce image noise, Ordered Subset Adaptive Steepest Descent Projection Onto Convex Sets (OS-ASD-POCS) algorithm[21] was employed to seek the optimal image $\vec{f}$ with respect to the following regularized L1 norm objective[32]:

$$\vec{f}^{\,*} = argmin\left|A\ \vec{f} - \tilde{g}_{data}\right| + \tau\left\|\vec{f}\right\|_{TV} \tag{7}$$

The first data fidelity term encourages consistency between measured projections and reconstructed image, where A is the system matrix and $\tilde{g}_{data}$ is the acquired post-correction CBCT projection. The second term penalizes total variation to encourage piecewise smoothness in the reconstructed image. The weight constant τ controls the tradeoff between these two terms. Implementation details and hyperparameters were provided in Section 2.8.

2.6.1. Implementation of OS-ASD-POCS in offset detector geometry—We observed that OS-ASD-POCS implementation may cause ring and streak artifacts in offset detector geometry (Fig. 3). These artifacts are caused by data inconsistency induced by scatter on the medial edge of the detector, where projection data is truncated due to 16 cm lateral offset in detector position (Fig. 4a). To demonstrate this problem, CBCT scans were acquired with various scatter suppression schemes (Fig. 3). When compared to 1D grid, 2D grid and additional residual scatter correction reduced ring and streak artifacts. However, such data inconsistency artifacts were not fully eliminated.

To address this issue, a projection-domain weighting scheme was implemented, where pixel-specific values of the data fidelity term were gradually reduced on the medial edge of the detector by applying multiplicative weights to pixel-by-pixel difference between experimentally acquired projection and forward projection of the image reconstruction at each iteration (Fig. 4b). These projection weights were identical to offset detector weights used in filtered backprojection reconstruction[23], following

$$w(t) = \frac{1}{2}\left(\sin\left(\frac{\pi \tan^{-1}\frac{t}{R}}{2\tan^{-1}\frac{\theta}{R}}\right) + 1\right), \qquad -\theta \le t \le \theta \tag{8}$$

where R is source to detector-distance, t is the spatial position of the detector and θ the corresponding smaller span of the array (Fig. 4a), It is important to emphasize that the purpose of offset detector weights in iterative reconstruction is different than the ones in filtered backprojection, where offset detector weights reduce the weight of detector pixels that double sample the central region of the object (red circle in Fig. 4a) due to offset detector geometry.

In iterative reconstruction, offset detector weights were applied to the pixels in the double sampled region during data fidelity term calculation (Fig. 5) to reduce data inconsistency in each iteration.

2.7. Image quality evaluations

First, all CBCT and MDCT image sets of any given phantom were rigidly co-registered. Subsequently, several image quality metrics were employed to benchmark the image quality of qCBCT against the clinical CBCT and MDCT. To evaluate the statistical significance of image quality differences between qCBCT and MDCT, we tested the null hypothesis that qCBCT HU accuracy metrics agree with the ones extracted from the reference MDCT. One-sided paired t-test was used at a significance level of $p = 0.05$, to the test the statistical significance of differences in HU loss and nonuniformity among imaging methods.

2.7.1. HU Loss—Object size dependent HU variations, or loss, were evaluated using two phantoms made from the same material in two different sizes,

$$\Delta HU_{method} = \left| HU_{small,\ method} - HU_{large,\ method} \right|$$

(9)

ΔHU_{method} is the average absolute HU difference between any method's HU values for the large and the small object made from the same material.

HU loss also depends on the material properties. ROI locations chosen for analyses were separated into two groups, one for soft-tissue-like and the other for bone-like regions in each phantom.

2.7.2. HU nonuniformity—Mean HU nonuniformity was defined as the absolute difference between the HU value of each ROI with respect to the ensemble mean of all ROIs in a CBCT image:

$$mean\ nonuniformity = \frac{1}{N}\sum_{i=1}^{N}\left|\overline{HU}(ROI(i)) - \left\{\frac{1}{N}\sum_{i=1}^{N}\overline{HU}(ROI(i))\right\}\right| \quad (10)$$

Where $\overline{HU}(ROI)$ is the average HU calculated in i^{th} ROI placed in the same phantom material. To calculate HU nonuniformity, a total of 20 ROIs were evenly distributed and selected in each transverse CBCT image's soft tissue-equivalent background.

2.7.3. Evaluation of low-contrast imaging performance—Low contrast imaging performance was evaluated by measuring relative CNR improvement, edge spread function in soft tissue mimicking object boundaries, and structure similarity index.

Relative change in CNR (rCNR) with respect to the images of the same phantom acquired in clinical mode using FDK (further explained in Section 2.8) was calculated as,

$$rCNR^{method}_{phantom,\ ROI(i)} = \frac{CNR^{\text{method}}_{phantom,\ ROI(i)}}{CNR^{Clinical\ FDK}_{phantom,\ ROI(i)}} \quad (11)$$

Where $CNR^{method}_{phantom,\ ROI(i)}$ represents the calculated CNR value for the data processing method of interest in $ROI(i)$ for each phantom. The ROIs were selected to span contrast objects in electron density and Catphan phantoms.

2.7.4. Modulation Transfer Function (MTF) and bar pattern analysis—One of the high contrast objects in the head-sized electron density phantom was used to measure MTF, and MTF was calculated using the method by Friedman et al[33]. Spatial frequency at 10% MTF level was used to compare spatial resolution. In addition, line-pair pattern module in small Catphan phantom was evaluated. The goal of MTF measurements was to show the noninferiority of spatial resolution in qCBCT images with respect to the MDCT and clinical CBCT images.

2.7.5. HU correlation histogram—The correlation of HU values between CBCT and MDCT images was investigated by pairing co-registered CBCT and MDCT image voxels

and generating HU correlation histograms. To establish a *reference* HU correlation between the two modalities, images of the head-sized electron density phantom were utilized, which were affected the least from scatter, beam hardening and image lag. As a first order approximation, the correlation between the HU values of CBCT and MDCT was assumed to be piecewise linear. Two separate linear fits were performed for CBCT-MDCT HU pairs, one for soft tissue-like materials and the other for bone-like materials. Mean and standard deviation of distance (error) between the HU values of CBCT images and the linear fit was calculated to quantify the CBCT HU inaccuracy for each phantom.

2.8. Experiment Setup

Two types of CBCT data were acquired using a TrueBeam linac mounted CBCT (Varian Medical Systems, Palo Alto, CA). First data set was acquired with our 2D antiscatter grid prototype and the proposed data processing pipeline, referred as “qCBCT”. A second data set was acquired using the standard Pelvis CBCT protocol, referred as “Clinical CBCT”.

Clinical CBCT scans were reconstructed using two different options[34].1) Standard reconstruction that employs FDK based filtered backprojection[35] and scatter correction based on scatter kernel superposition[15]. 2) An iterative reconstruction method combined with a more robust scatter correction algorithm that solves Boltzmann transport equation[14]. These methods were referred as Clinical FDK and Clinical IR, respectively.

Likewise, qCBCT images were reconstructed using the FDK algorithm and iterative reconstruction, which were referred as qCBCT FDK and qCBCT IR, respectively. In qCBCT IR, hyperparameters were tuned to achieve noninferior spatial resolution with respect to clinical CBCT and MDCT images while maximizing CNR[36,37]. A zero-value image was used for initialization. In each iteration, a subset of $blocksize = 50$ projection views were used to approximate the gradient of the cost function. We count one iteration after all 900 projections were used with $\frac{900}{50} = 18$ sub-iterations. Overall, $iter = 50$ POCS/descent iterations were used. In each iteration, the image update coefficient factor was set to be $\lambda = 1$ without any reduction factor for a faster convergence. The TV-steepest descent step size was initialized to $\alpha = 0.002$ and executed for $TV_{iter} = 15$ times when the change in the image due to TV-steepest descent is assessed. If this change exceeded $r_{max} = 0.94$ times data fidelity POCS based update, the TV-steepest descent step size is reduced by $\alpha_{red} = 0.95$. The implementation was performed with the TIGRE MATLAB/CUDA toolbox with GPU acceleration[22].

Both qCBCT and clinical CBCT datasets were acquired using the same Pelvis CBCT protocol parameters in offset detector geometry (i.e., half fan geometry). 900 projections were acquired with a bow tie filter and 0.89 mm titanium beam filter in place, and detector pixel size was 0.388×0.388 mm^2. Scans were acquired at 125 kVp and 1080 mAs, except for the pelvis phantoms which were acquired at 140kVp and 1680 mAs. qCBCT and clinical CBCT were reconstructed using 0.9×0.9×2 mm^3 and 0.908×0.908×1.98 mm^3 voxel size, respectively.

Focused tungsten 2D antiscatter grid prototype had a grid ratio of 12, grid pitch of 2 mm, and septal thickness of 0.1 mm, designed for offset detector CBCT geometry in TrueBeam[38]. The 2D grid was installed on the FPD, after removing the default (1D) antiscatter grid.

Effects of scattered radiation and CBCT image quality strongly depend on the object size and composition. Therefore, experiments were conducted using 7 different phantoms spanning from 20 cm diameter head sized phantoms to a large pelvis phantom with a lateral dimension of 55 cm. Anatomically more realistic thorax and pelvis phantoms were also employed.

Finally, a third set of image data was acquired with the MDCT (Philips Brilliance Big Bore 16 slice MDCT, Netherlands) which served as the gold standard reference[39]. Images were acquired using $0.9\times0.9\times3$ mm^3 voxel size. MDCT scans were acquired in helical mode using 120 kVp and 140 kVp (for pelvis phantom scans). For both CBCT and MDCT scans, CTDI values were 16 mGy and 37 mGy for low and high kVp scans, respectively.

3. Results

3.1. Effect of data processing pipeline on qCBCT image quality

Effect of the data processing pipeline steps is shown in Fig. 6. When only 2D grid was utilized, periphery of the phantom had lower HU values than the center (blue arrows), largely due to increased scatter-to-primary ratio (SPR) in peripheral regions by the bow tie filter. Residual scatter also caused dark streaks between high density objects and ring artifacts in the central region (yellow arrow).

While most shading and ring artifacts were suppressed after scatter correction, other artifacts are still visible, such as image lag artifacts in the periphery (black arrow). Central section of the phantom body has higher HU values mostly due to beam hardening introduced by the bow tie filter. After image lag correction, median image HU nonuniformity in the radar artifact region was reduced from 16 to 4 HU (Fig.7a). Likewise, beam hardening correction reduced median HU nonuniformity between the center and periphery from 43 HU to 5 HU (Fig. 7b).

Using OS-ASD POCS without offset detector weights reduced stochastic noise but introduced ring and streak artifacts due to data inconsistency at the truncated edge of the detector. Application of the proposed offset detector weights eliminated these artifacts.

3.2. Qualitative evaluation of qCBCT image quality

Image quality differences between qCBCT and clinical CBCT images were comparable in head sized phantoms due to lower SPR (Fig. 8). Relatively less streak artifacts between high density objects in qCBCT images were due to robust scatter suppression in qCBCT images.

The importance of robust data correction was evident in larger phantoms. Clinical IR images have less artifacts than Clinical FDK in large phantoms with heterogenous material composition. qCBCT FDK further improved HU accuracy and reduced artifacts across all

phantoms. qCBCT FDK and IR images have similar HU values, but less noise was observed in qCBCT IR.

In visual comparisons of pelvis and large pelvis phantoms (Fig. 8, last two rows), CT number degradation in bony anatomy is evident in Clinical FDK images. While qCBCT significantly reduces HU degradation, they also appear noisier than Clinical CBCT images. This is due to low primary fluence transmitted through the large pelvis phantom and relatively high residual SPR despite the 2D Grid, which causes noise amplification after scatter correction.

Ring artifacts in the outer region of the phantoms in qCBCT images (red arrows, Fig. 8) are due to flickering detector pixels (pixel values are substantially lower or higher than expected in a certain pixel value range) when 2D grid was present. The cause of this issue needs further investigation. In the qCBCT IR images of the standard pelvis phantom, HU values were different in bone and soft tissue interfaces (blue arrow, Fig. 8). This is caused by 2×7 pixel binning in projections. Iterative reconstruction aims to preserve possible edges while smoothing homogeneous areas. When using large pixels, volume averaging problems can be exacerbated by the iterative reconstruction process, which may lead to artifacts in bone-soft tissue interfaces. We have not observed such artifacts when using smaller pixel sizes.

3.2.1. HU Loss—Average HU loss in soft tissue equivalent sections of the electron density phantom was 62, 22, 7, and 5 HU for Clinical FDK, Clinical IR, qCBCT IR, and MDCT images, respectively (Fig. 9a). HU loss in qCBCT and MDCT images were similar in electron density phantoms, implying that qCBCT can provide comparable HU accuracy to MDCT.

Average HU loss for bone-like objects was significantly higher; it was 170, 120, 43, and 38 HU for Clinical FDK, Clinical IR, qCBCT IR, and MDCT images, respectively (Fig. 9d). Differences in HU loss between qCBCT FDK and IR images were within 1HU.

For Catphan phantoms, differences in HU loss were smaller between Clinical and qCBCT images (Fig. 9b and 9e). For the Clinical FDK, Clinical IR, qCBCT IR, and MDCT images, the average Hounsfield unit (HU) loss in soft tissue equivalent sections was 37, 17, 15, and 7 HU, respectively (Fig. 9c). In bone-mimicking sections, the average HU loss was 46, 27, 13, and 15 HU for Clinical FDK, Clinical IR, qCBCT IR, and MDCT images, respectively (Fig. 9f).

When compared to MDCT, HU loss p values for qCBCT and clinical CBCT IR were 0.5 and 2e-11 in electron density phantoms, respectively. In pelvis phantoms, HU loss p values for qCBCT and clinical CBCT IR were 0.77 and 0.009, respectively. These results imply that HU loss differences between MDCT and qCBCT were not statistically significant. For Catphan phantoms, HU loss p values for qCBCT and clinical CBCT IR were 7e-4 and 1e-7, respectively. While, these differences are statistically significant, HU loss in qCBCT has better agreement with MDCT than clinical CBCT IR images.

3.2.2. HU nonuniformity—Similar to the trends in HU loss, HU nonuniformity in qCBCT was substantially less than Clinical CBCT, and particularly in pelvis-sized phantoms

(Table 1 and Fig. 10b); mean nonuniformity across all phantoms was 32, 23, 10, 10, and 6 HU for Clinical FDK, Clinical IR, qCBCT FDK, qCBCT IR, and MDCT images, respectively. However, large ROI-to-ROI HU deviations were observed in a small subset of ROIs due to image artifacts, particularly in clinical CBCT images. For example, maximum ROI-to-ROI HU deviation was 193 HU in Clinical FDK images of the pelvis electron density phantom. Such ROI-to-ROI deviations were only 15 HU in qCBCT FDK images.

3.2.3. Low contrast imaging performance—Mean rCNR in Clinical IR images was in the range of 1.1 – 1.8 in head sized phantoms (Fig. 11). Mean rCNR in qCBCT FDK images was in the range of 1–1.4 respectively, indicating that qCBCT FDK provides modest improvement in CNR with respect to Clinical FDK images. rCNR in qCBCT IR images were 1.4 – 2.4, indicating that qCBCT can offer substantial CNR improvement using OS-ASD-POCS reconstruction algorithm, due to reduction in noise (Fig. 11a).

3.2.4. Spatial resolution characteristics—Overall, spatial resolution of qCBCT was noninferior to Clinical CBCT and MDCT images (Fig.12a). The values of MTF at 10% level for Clinical FDK, Clinical IR, qCBCT FDK, and qCBCT IR were 0.39, 0.41, 0.43, and 0.42 mm^{-1}, respectively. 10% MTF level in MDCT images was 0.37 mm^{-1}. In bar pattern phantom images, 3, 4, and 5 line pairs per cm were differentiated in MDCT, Clinical CBCT, and qCBCT images, respectively.

3.2.5. HU correlation histograms—Trends in CBCT-MDCT HU correlation histograms agreed with HU loss and nonuniformity evaluations. In soft tissue-mimicking regions of head sized phantoms, HU values for CBCT and MDCT were highly correlated due to highly accurate raw data and lower noise (Fig. 13a).

Mean error (Tables 2 and 3) values were in the range of 6 – 105 HU for Clinical CBCT images, whereas mean error was in the range of 5–35 HU for qCBCT images. Merging all HU correlation histograms into one composite histogram better visualizes the dispersion of CBCT HU values (Fig. 13).

HU correlation degraded substantially for bone-like regions in Clinical FDK images (Fig. 13), indicating the challenges in improving raw data fidelity in high SPR conditions. qCBCT images preserved the expected linear behavior of HU values when compared to Clinical CBCT images. Mean errors across all phantoms for Clinical FDK, Clinical IR, qCBCT FDK, and qCBCT IR were 22, 16, 15, and 10 HU for soft tissue-mimicking regions (Table 2) and 63, 49, 23 and 19 HU for bone-mimicking regions (Table 3), respectively. While noise reduction in qCBCT IR helped to improve HU correlation, improvement of raw data fidelity was the key factor in achieving higher qCBCT-MDCT HU correlation.

Except for the Catphan phantom, HU correlation errors in large phantoms were significantly less in qCBCT than the ones in Clinical CBCT images (p value < 0.05). In small phantoms, statistically significant HU correlation errors between qCBCT and clinical CBCT were not observed.

4. Discussion

While the performance of 2D grids in CBCT imaging has been investigated previously[6,8,38], HU accuracy and CNR improvement was limited due to lack of key raw data correction and image denoising methods. In this work, we presented a raw data correction and iterative reconstruction pipeline with 2D antiscatter grids, referred to as qCBCT, which further improves quality of CBCT images.

Even though scatter rejection and correction are the primary factors in achieving high image quality in qCBCT, they are not sufficient to achieve high HU accuracy comparable to MDCT. For example, localized HU nonuniformities in the periphery of the pelvis electron density phantom were 15 – 46 HU due to image lag and beam hardening. After beam hardening and image lag correction, HU nonuniformity was down 8 HU on average, indicating the essence of complete raw data correction chain for quantitatively accurate CBCT images.

Regarding HU accuracy, qCBCT provided statistically significant improvements over both Clinical CBCT imaging methods investigated. Since both qCBCT and Clinical CBCT utilize beam hardening and image lag correction methods, improved image quality in qCBCT was attributed to 2D antiscatter grids and Grid-based Scatter Sampling. Even though 2D grid does not eliminate all scatter, the remaining smaller amount of scatter can be more easily corrected with a scatter correction method. Conventional radiographic antiscatter grid in Clinical CBCT transmits a larger fraction of scatter fluence to the detector and makes residual scatter correction a more challenging task. Our results also reaffirm that Clinical IR has significantly better scatter correction performance than the scatter kernel superposition-based method used in Clinical FDK images.

In contrast to model-based patient scatter correction where glare/backscatter is not modeled and calls for further glare correction such as the deconvolution-based methods[40]. The Grid-based scatter sampling method used in this work is a measurement-based scatter correction method that corrects the cumulative effects of all forms of scatter, including glare and detector backscatter without explicitly addressing each individual component. It is desirable to characterize the magnitude of any remaining glare or backscatter and perform further correction when needed.

Aggregate evaluations across all ROIs and phantoms showed that the HU loss differences between qCBCT and MDCT were small, suggesting comparable HU accuracy in both imaging modalities. However, MDCT images had slightly fewer artifacts, particularly in larger phantoms. These small differences could be attributed to suboptimal scatter suppression, beam hardening, and lag correction, as well as the limitations of FPD technology. For example, primary x-ray fluence was attenuated 4–5 orders of magnitude in large, bone-containing phantoms. At such low signal levels, limited dynamic range and relatively high electronic noise in FPDs[41] may challenge raw data correction and accurate measurement of primary signals. These issues are further amplified by relatively low quantum efficiency of FPDs and associated quantum noise in primary signal.

Given that the 2D antiscatter grid in qCBCT has higher primary transmission than the radiographic grid used in clinical CBCT (85% versus 70%)[8,38], and better scatter rejection performance, one would expect to achieve higher CNR in qCBCT than Clinical CBCT images. Several factors might have contributed to this discrepancy. First, measured CNR is sensitive to spatial resolution properties. qCBCT FDK images had slightly higher spatial resolution than Clinical CBCT images (Fig. 12). If spatial resolution properties of qCBCT and Clinical CBCT images are matched better, CNR in qCBCT images can be improved further. Second, qCBCT images did not employ any high spatial frequency artifact reduction algorithms, such as ring artifact correction methods, as in Clinical CBCT. Such high frequency artifacts can increase noise and reduce CNR. Implementation of such artifact reduction methods in qCBCT will be an area of future investigations.

Scatter rejection by 2D grid and residual scatter correction with the GSS method improve contrast but also amplify noise in CBCT images[6]. Despite noise reduction with OS-ASD-POCS, qCBCT images of large phantoms appear noisier than MDCT and on par with Clinical CBCT, which imply the need for improved noise reduction in qCBCT.

This work emphasizes the importance of phantom size and composition in CBCT image quality evaluations. Image quality differences among all imaging methods were generally small in 20 cm diameter phantoms, because the effects of scatter, beam hardening, and image lag are less in such phantoms. When human torso sized phantoms with bony structures were used, HU loss exceeded 100 HU. Hence, the use of standard head-sized phantoms and absence of bone-like embedded objects in CBCT image quality evaluations may not fully reveal the extent of image quality issues in CBCT images[16,42].

There are several factors that may impact the performance of the proposed pipeline. Firstly, long-term variations in gantry flex could cause suboptimal suppression of grid artifacts, leading to the introduction of fixed pattern noise, or ring artifacts. Although we did not observe major detrimental effects of gantry flex, further investigations are needed to assess the impact of long-term gantry flex variations. Secondly, residual scatter measurement in very large phantoms is challenging due to the very low primary signal levels, which may introduce errors in scatter estimation. Thirdly, while the use of a 2D grid provides higher average primary transmission (>80%), the primary signal in grid shadows is lower than that in the grid holes. This may amplify the effects of additive electronic noise in pixels residing in grid shadows and requires further investigation. Lastly, the image quality metrics utilized in this study do not fully depict the impact of qCBCT on clinical tasks in CBCT-guided radiation therapy. For example, improved CNR in relatively uniform phantoms as in our study may not warrant improved visualization of anatomical structure boundaries in CBCT images. Further research is required to investigate the effects of qCBCT on specific clinical tasks, such as online dose calculations, radiomics feature extraction, and improved visualization during localization.

5. Conclusion

The utilization of a 2D antiscatter grid and grid-based scatter sampling in combination with other raw data correction methods and an iterative reconstruction method has been shown to

significantly improve the quality of CBCT images used in radiation therapy. Specifically, the Hounsfield unit (HU) accuracy in qCBCT images approaches the HU accuracy of the gold standard MDCT images.

From a qualitative perspective, improved image quality in qCBCT may increase the clinician's confidence during target localization in image-guided radiation therapy. From a quantitative imaging perspective, qCBCT images have the potential to be used for CBCT-based dose calculations during treatment delivery to either confirm delivered dose or support decisions for plan adaptation. Furthermore, anatomical changes and treatment response over the course of treatment can be potentially better assessed in qCBCT images.

Acknowledgements

This work was funded in part by grants from NIH/NCI R21CA198462 and R01CA245270.

References

1. Simpson DR, Lawson JD, Nath SK, Rose BS, Mundt AJ, Mell LK. A survey of image-guided radiation therapy use in the United States. Cancer. 2010;116(16):3953–3960. [PubMed: 20564090]
2. Liu Y, Shi H, Huang S, et al. Early prediction of acute xerostomia during radiation therapy for nasopharyngeal cancer based on delta radiomics from CT images. Quantitative imaging in medicine and surgery. 2019;9(7):1288. [PubMed: 31448214]
3. Delgadillo R, Spieler BO, Ford JC, et al. Repeatability of CBCT radiomic features and their correlation with CT radiomic features for prostate cancer. Medical physics. 2021;48(5):2386–2399. [PubMed: 33598943]
4. Fave X, Mackin D, Yang J, et al. Can radiomics features be reproducibly measured from CBCT images for patients with non-small cell lung cancer? Medical physics. 2015;42(12):6784–6797. [PubMed: 26632036]
5. Gingold E Cone Beam Computed Tomography, Editor: Shaw Chris. Series:"Imaging in Medical Diagnosis and Therapy," Hendee W, Series Editor. CRC Press, Taylor & Francis Group, Boca Raton, FL, 2014. Hardcover 273 pp. Price: $188.00. ISBN: 9781439846261. In.: Wiley Online Library; 2019.
6. Altunbas C, Park Y, Yu Z, Gopal A. A unified scatter rejection and correction method for cone beam computed tomography. Medical Physics. 2021;48(3):1211–1225. [PubMed: 33378551]
7. Park Y, Alexeev T, Miller B, Miften M, Altunbas C. Evaluation of scatter rejection and correction performance of 2D antiscatter grids in cone beam computed tomography. Medical Physics. 2021;48(4):1846–1858. [PubMed: 33554377]
8. Altunbas C, Kavanagh B, Alexeev T, Miften M. Transmission characteristics of a two dimensional antiscatter grid prototype for CBCT. Medical physics. 2017;44(8):3952–3964. [PubMed: 28513847]
9. Park Y, Miller B, Kavanagh B, Miften M, Altunbas C. Improving CBCT Image Quality for Obese Patients Using Unified Scatter Rejection and Correction Method. MEDICAL PHYSICS. 2020;47(6):E395–E395.
10. Bayat F, Eldib ME, Altunbas C. Megavoltage cross-scatter rejection and correction using 2D antiscatter grids in kilovoltage CBCT imaging. Medical Imaging 2022: Physics of Medical Imaging. 2022;12031:387–395.
11. Bayat F, Eldib ME, Kavanagh B, Miften M, Altunbas C. Concurrent kilovoltage CBCT imaging and megavoltage beam delivery: suppression of cross-scatter with 2D antiscatter grids and grid-based scatter sampling. Physics in Medicine & Biology. 2022;67(16):165005.
12. Alexeev T, Kavanagh B, Miften M, Altunbas C. Two-dimensional antiscatter grid: A novel scatter rejection device for Cone-beam computed tomography. Medical physics. 2018;45(2):529–534. [PubMed: 29235120]

13. Yu Z, Park Y, Altunbas C. Simultaneous scatter rejection and correction method using 2D antiscatter grids for CBCT. Paper presented at: Medical Imaging 2020: Physics of Medical Imaging2020.
14. Wang A, Maslowski A, Messmer P, et al. Acuros CTS: A fast, linear Boltzmann transport equation solver for computed tomography scatter–Part II: System modeling, scatter correction, and optimization. Medical physics. 2018;45(5):1914–1925. [PubMed: 29509973]
15. Sun M, Nagy T, Virshup G, Partain L, Oelhafen M, Star-Lack J. Correction for patient table-induced scattered radiation in cone-beam computed tomography (CBCT). Medical physics. 2011;38(4):2058–2073. [PubMed: 21626939]
16. Cai B, Laugeman E, Mazur TR, et al. Characterization of a prototype rapid kilovoltage x-ray image guidance system designed for a ring shape radiation therapy unit. Medical physics. 2019;46(3):1355–1370. [PubMed: 30675902]
17. Stankovic U, van Herk M, Ploeger LS, Sonke JJ. Improved image quality of cone beam CT scans for radiotherapy image guidance using fiber-interspaced antiscatter grid. Medical physics. 2014;41(6Part1):061910. [PubMed: 24877821]
18. Wu P, Sisniega A, Stayman J, et al. Cone-beam CT for imaging of the head/brain: development and assessment of scanner prototype and reconstruction algorithms. Medical physics. 2020;47(6):2392–2407. [PubMed: 32145076]
19. Sisniega A, Zbijewski W, Xu J, et al. High-fidelity artifact correction for cone-beam CT imaging of the brain. Physics in Medicine & Biology. 2015;60(4):1415. [PubMed: 25611041]
20. Ohnesorge B, Flohr T, Schwarz K, Heiken J, Bae K. Efficient correction for CT image artifacts caused by objects extending outside the scan field of view. Medical physics. 2000;27(1):39–46. [PubMed: 10659736]
21. Qiao Z A simple and fast ASD-POCS algorithm for image reconstruction. Journal of X-Ray Science and Technology. 2021;29(3):491–506. [PubMed: 33843721]
22. Biguri A, Dosanjh M, Hancock S, Soleimani M. TIGRE: a MATLAB-GPU toolbox for CBCT image reconstruction. Biomedical Physics & Engineering Express. 2016;2(5):055010.
23. Wang G X-ray micro-CT with a displaced detector array. Medical physics. 2002;29(7):1634–1636. [PubMed: 12148746]
24. Siewerdsen J, Jaffray D. A ghost story: Spatio-temporal response characteristics of an indirect-detection flat-panel imager. Medical physics. 1999;26(8):1624–1641. [PubMed: 10501063]
25. Mail N, Moseley D, Siewerdsen J, Jaffray D. An empirical method for lag correction in cone-beam CT. Medical physics. 2008;35(11):5187–5196. [PubMed: 19070253]
26. Starman J, Star-Lack J, Virshup G, Shapiro E, Fahrig R. Investigation into the optimal linear time-invariant lag correction for radar artifact removal [published online ahead of print 2011/07/23]. Medical Physics. 2011;38(5):2398–2411. [PubMed: 21776774]
27. Alexeev T, Kavanagh B, Miften M, Altunbas C. Development and Evaluation of a Total Variation Minimization Based Method for Suppressing Ring Artifacts in CBCT Images. MEDICAL PHYSICS. 2018;45(6):E536–E536.
28. Hsieh J Computed tomography: principles, design, artifacts, and recent advances. 2003.
29. Maslowski A, Wang A, Sun M, Wareing T, Davis I, Star-Lack J. Acuros CTS: A fast, linear Boltzmann transport equation solver for computed tomography scatter–Part I: Core algorithms and validation. Medical physics. 2018;45(5):1899–1913. [PubMed: 29509970]
30. Punnoose J, Xu J, Sisniega A, Zbijewski W, Siewerdsen J. spektr 3.0—A computational tool for x-ray spectrum modeling and analysis. Medical physics. 2016;43(8Part1):4711–4717. [PubMed: 27487888]
31. Joseph PM, Spital RD. A method for correcting bone induced artifacts in computed tomography scanners. Journal of computer assisted tomography. 1978;2(1):100–108. [PubMed: 670461]
32. Sidky EY, Pan X. Image reconstruction in circular cone-beam computed tomography by constrained, total-variation minimization. Physics in Medicine & Biology. 2008;53(17):4777. [PubMed: 18701771]
33. Friedman SN, Fung GS, Siewerdsen JH, Tsui BM. A simple approach to measure computed tomography (CT) modulation transfer function (MTF) and noise-power spectrum (NPS)

using the American College of Radiology (ACR) accreditation phantom. Medical physics. 2013;40(5):051907. [PubMed: 23635277]

34. Systems VM. TrueBeam Technical Reference Guide—Volume 2: Imaging. 2013.
35. Feldkamp LA, Davis LC, Kress JW. Practical cone-beam algorithm. Josa a. 1984;1(6):612–619.
36. Tang J, Nett BE, Chen G-H. Performance comparison between total variation (TV)-based compressed sensing and statistical iterative reconstruction algorithms. Physics in Medicine & Biology. 2009;54(19):5781. [PubMed: 19741274]
37. Penfold S, Schulte RW, Censor Y, Rosenfeld AB. Total variation superiorization schemes in proton computed tomography image reconstruction. Medical physics. 2010;37(11):5887–5895. [PubMed: 21158301]
38. Altunbas C, Alexeev T, Miften M, Kavanagh B. Effect of grid geometry on the transmission properties of 2D grids for flat detectors in CBCT. Physics in Medicine & Biology. 2019;64(22):225006. [PubMed: 31585444]
39. Brink JA, Heiken JP, Wang G, McEnery KW, Schlueter FJ, Vannier M. Helical CT: principles and technical considerations. Radiographics. 1994;14(4):887–893. [PubMed: 7938775]
40. Poludniowski G, Evans PM, Kavanagh A, Webb S. Removal and effects of scatter-glare in cone-beam CT with an amorphous-silicon flat-panel detector. Physics in Medicine and Biology. 2011;56(6):1837–1851. [PubMed: 21358018]
41. Colbeth RE, Mollov IP, Roos PG, Shapiro EG. Flat panel CT detectors for sub-second volumetric scanning. Medical Imaging 2005: Physics of Medical Imaging. 2005;5745:387–398.
42. Mao W, Liu C, Gardner SJ, et al. Evaluation and clinical application of a commercially available iterative reconstruction algorithm for CBCT-based IGRT. Technology in cancer research & treatment. 2019;18:1533033818823054. [PubMed: 30803367]

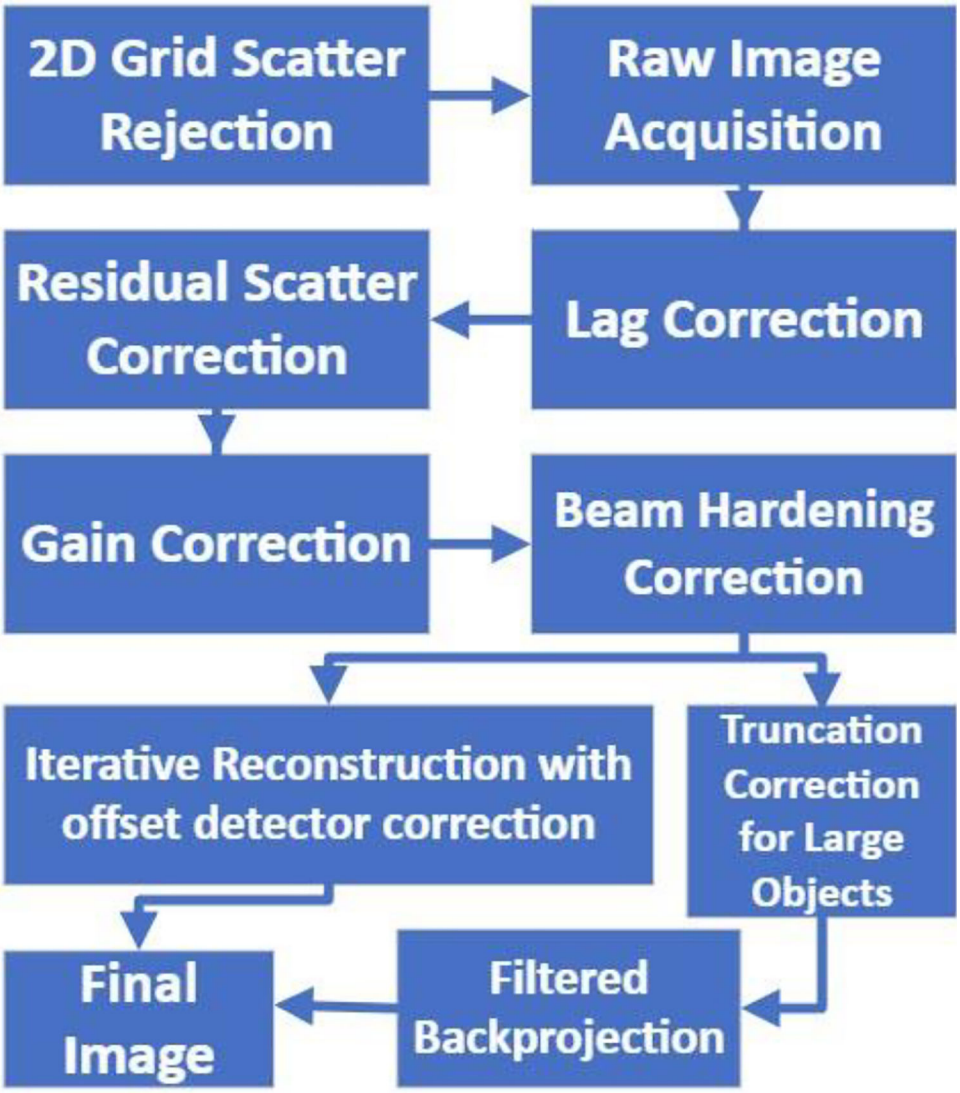

Fig.1.
Raw Data Correction and Iterative Reconstruction Pipeline for qCBCT scans acquired with 2D antiscatter grid.

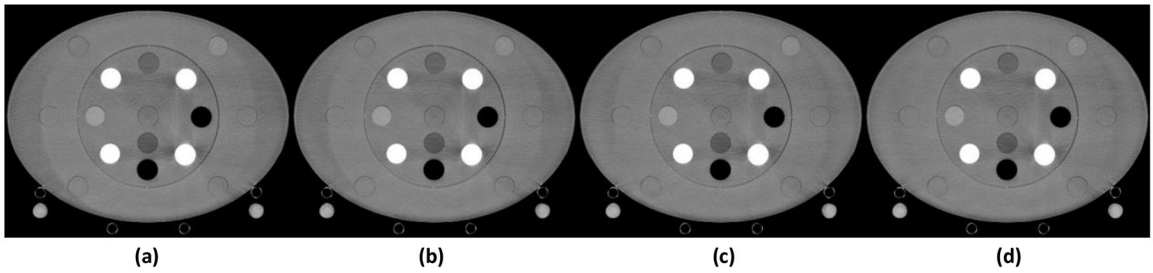

Fig. 2:
Image lag correction for (a) M=50 (b) M=100 (c) M=200 and (d) M=300 over 16 averaged slices. HU Window=[−250 250].

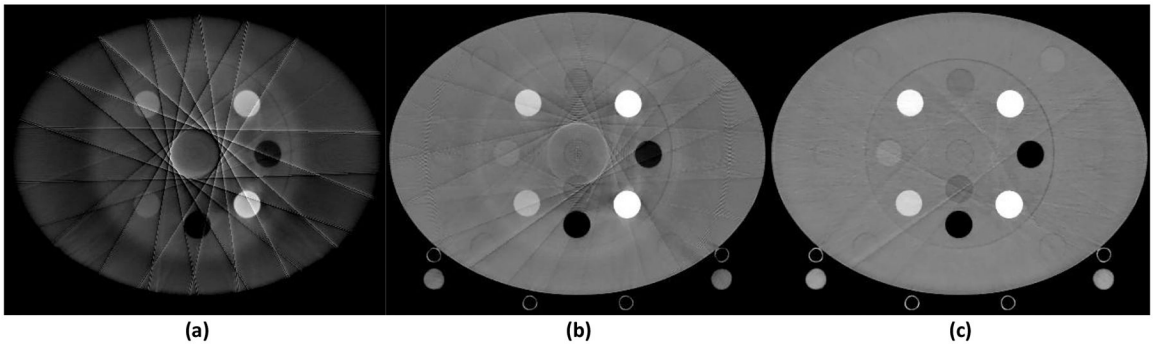

Fig.3.

CBCT scans were acquired using offset detector geometry and reconstructed using OS-ASD-POCS with (a) 1D antiscatter grid (b) 2D antiscatter grid (c) 2D antiscatter grid + GSS scatter correction. When scatter is present, projection truncation due to offset detector geometry causes ring and streak artifacts due to data inconsistency at the truncated edge of the detector. The use of 2D grid instead of 1D grid reduces these artifacts. 2D grid and residual scatter correction substantially reduce artifacts, but artifacts are not fully eliminated. HU window= [−500 500].

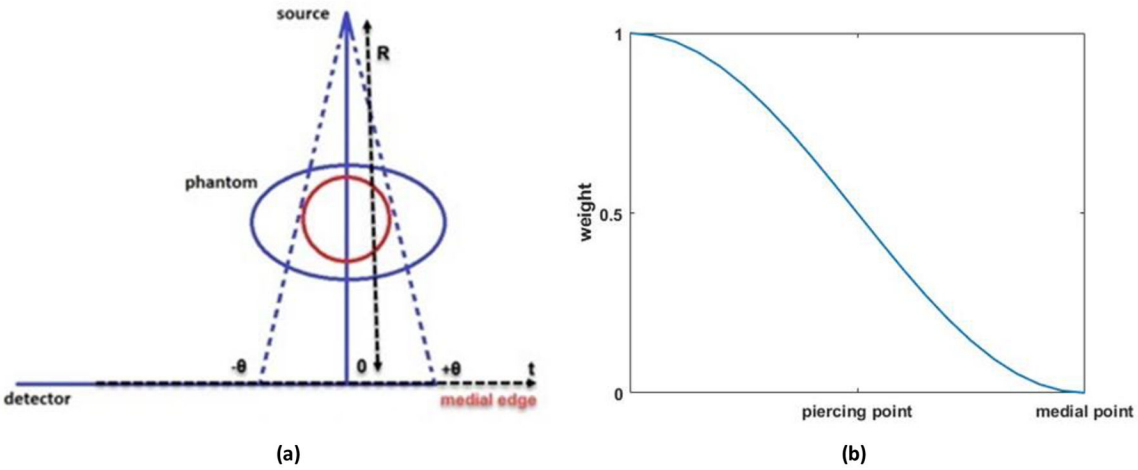

Fig.4.

(a), Offset detector geometry used in the CBCT experiments. Medial edge of the projection is closest to the piercing point and the object is truncated, which causes data inconsistency when scatter is present. (b), data inconsistency is reduced by applying correction weights to the fidelity term of pixels within 4 cm of the piercing point.

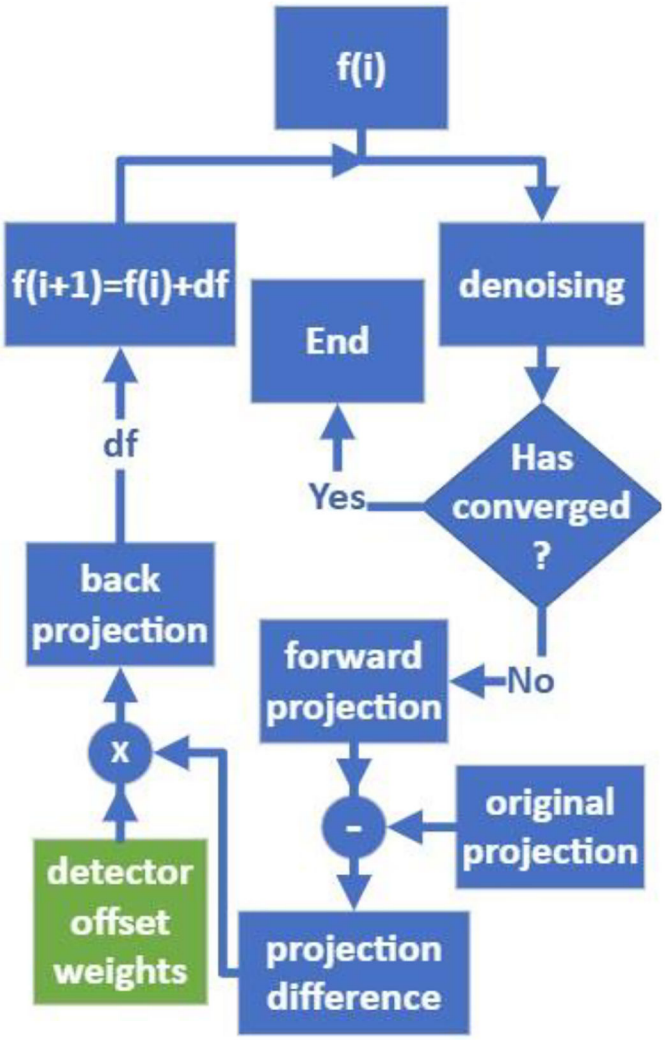

Fig.5.
Flowchart for updated iterative reconstruction step to account for scatter induced data inconsistency and associated ring artifacts.

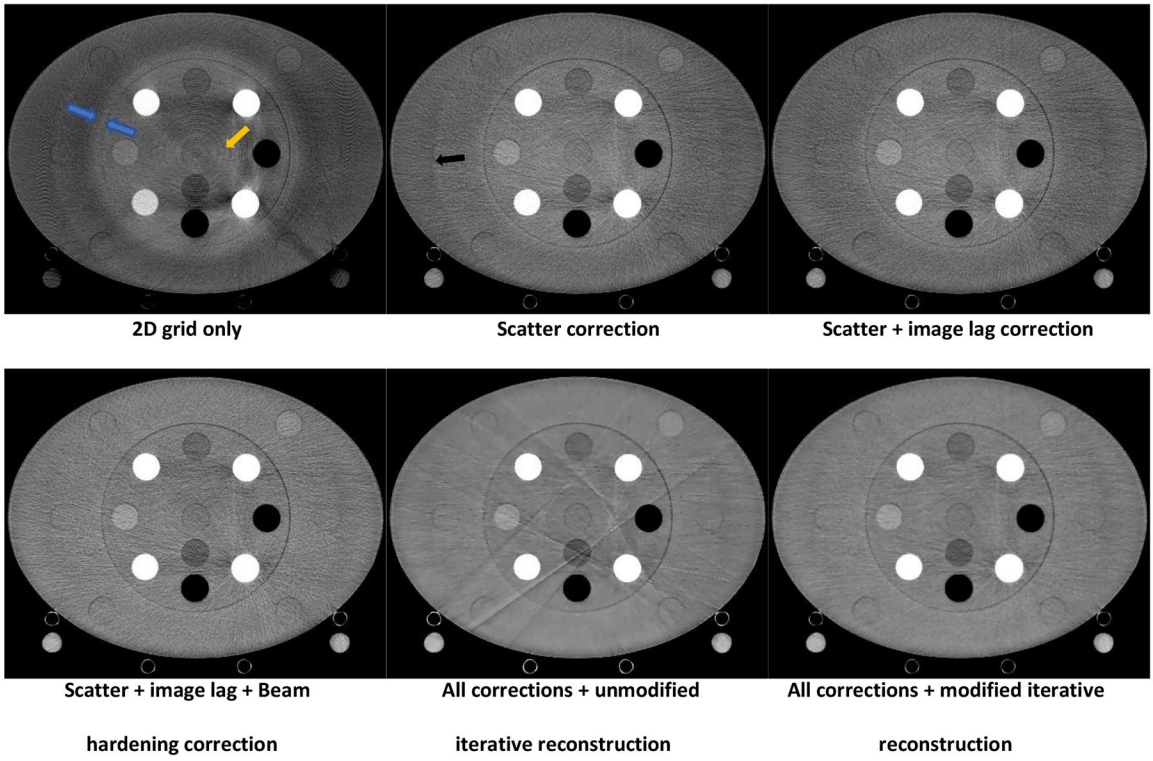

Fig.6.

Effect of the data processing pipeline steps on qCBCT image quality. Blue arrows: transition zone between the peripheral shading artifacts caused by bow tie filter and the central region. Yellow arrow: Ring artifacts caused by residual scatter and associated suboptimal gain correction. Balck arrow: Radar or image lag artifacts. Window = [−250 250].

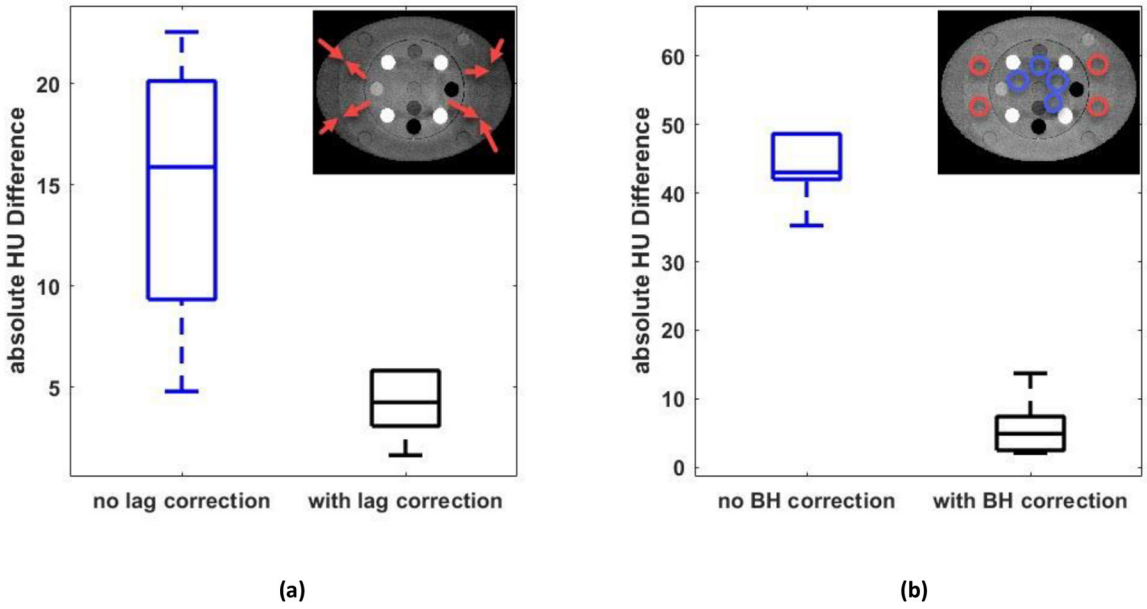

Fig.7.

Effects of image lag and beam hardening correction are show in (a) and (b), respectively. ROI locations for image lag induced HU nonuniformity calculations were indicated by red arrows. ROI locations for beam hardening induced HU nonuniformity calculations were indicated with circles. Central mark indicates the median, and the bottom and top edges of the box indicate the 25th and 75th percentiles, respectively. Whiskers extend to the most extreme data points not considered outliers, and the outliers (if available) are plotted individually using the '+' marker symbol. Window = [−250 250].

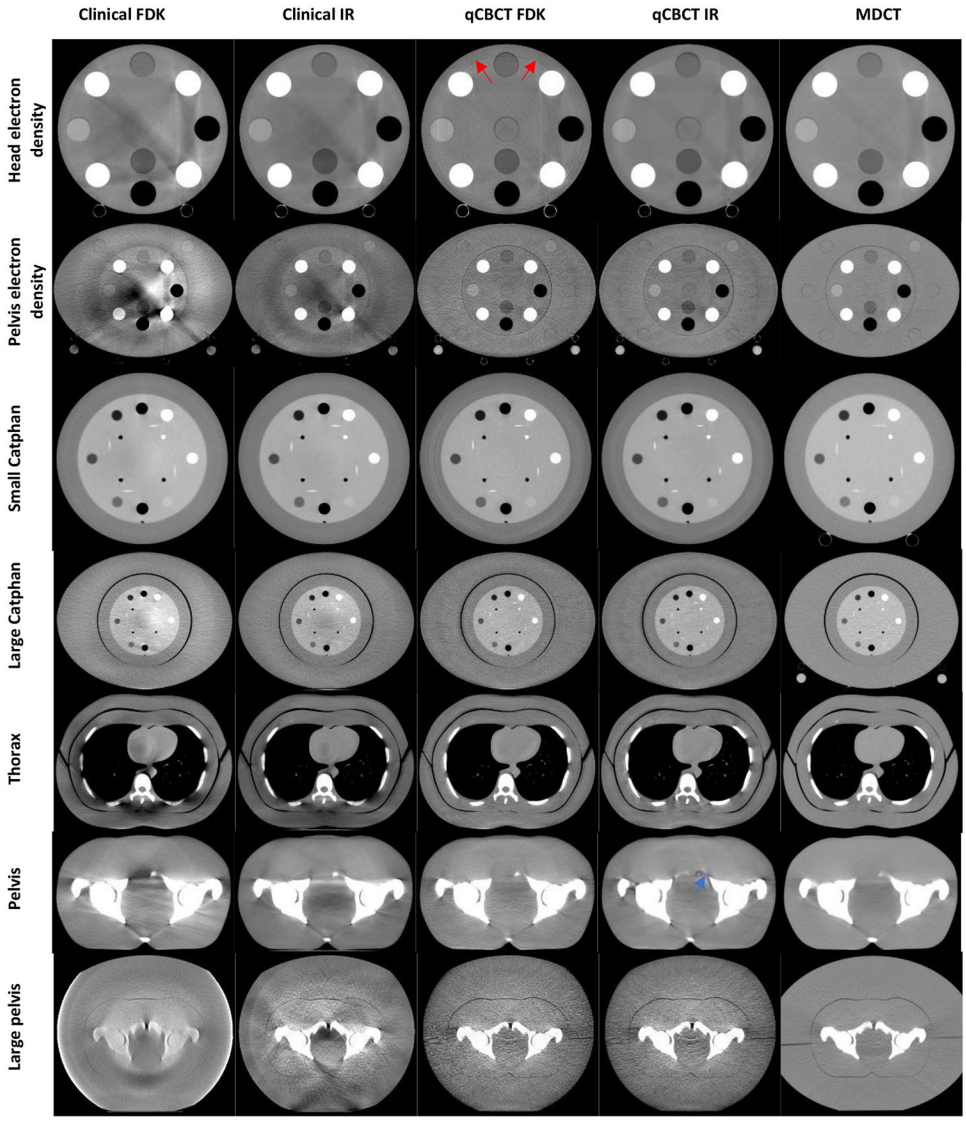

Fig.8.

Images of 7 phantoms acquired with all 5 CBCT and MDCT methods. Ring artifacts in the periphery of head qCBCT images (red arrows) are caused by the detector readout. Differences in bone - soft tissue interface in the qCBCT IR pelvis phantom (blue arrow) was caused by pixel binning in projections. HU window is [−250 250] for all phantoms except obese pelvis which has a HU window of [−500 500].

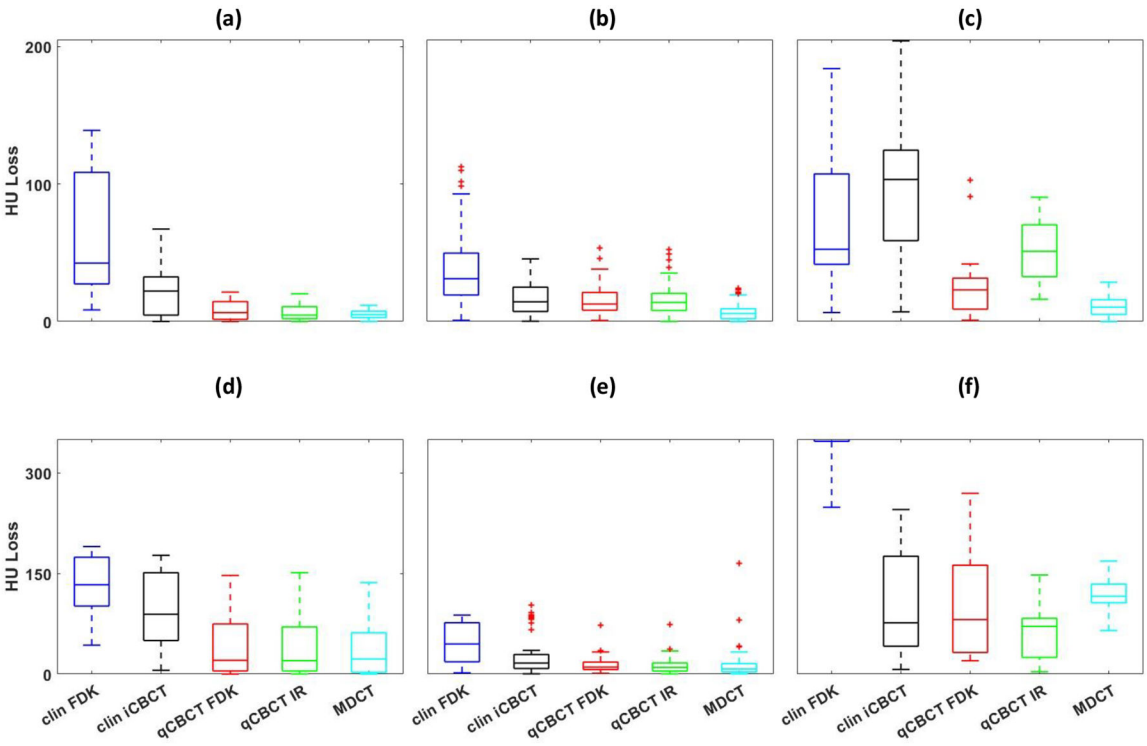

Fig. 9.

HU loss for (a) water-equivalent background and (d) bone-like objects for head and pelvis-sized electron density phantoms, (b) water-equivalent background and (e) bone-like objects for small and large Catphan and (c) water-equivalent background and (f) bone-like objects for small and large pelvis. Central mark indicates the median, and the bottom and top edges of the box indicate the 25th and 75th percentiles, respectively. Whiskers extend to the most extreme data points not considered outliers, and the outliers (if available) are plotted individually using the '+' marker symbol.

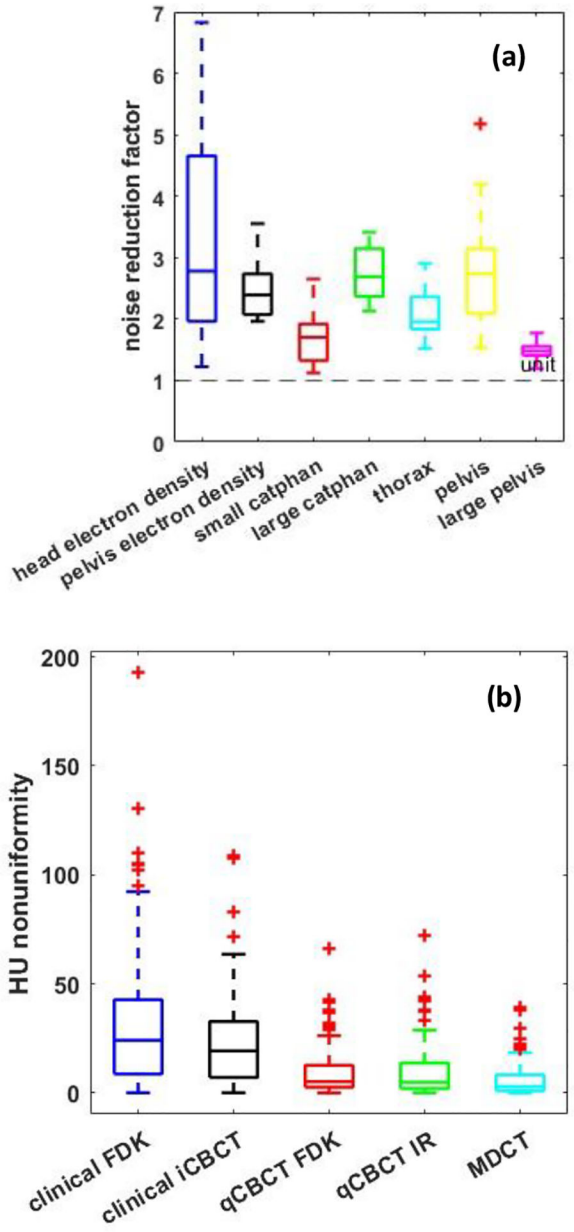

Fig. 10.

(a) noise reduction factor for qCBCT IR with respect to qCBCT FDK and (b) HU nonuniformity as a function of CBCT imaging methods. Centerline, box, and whiskers represent median, 25–75 quartile, and most extreme data points not considered outliers, respectively. The outliers are presented by crosses.

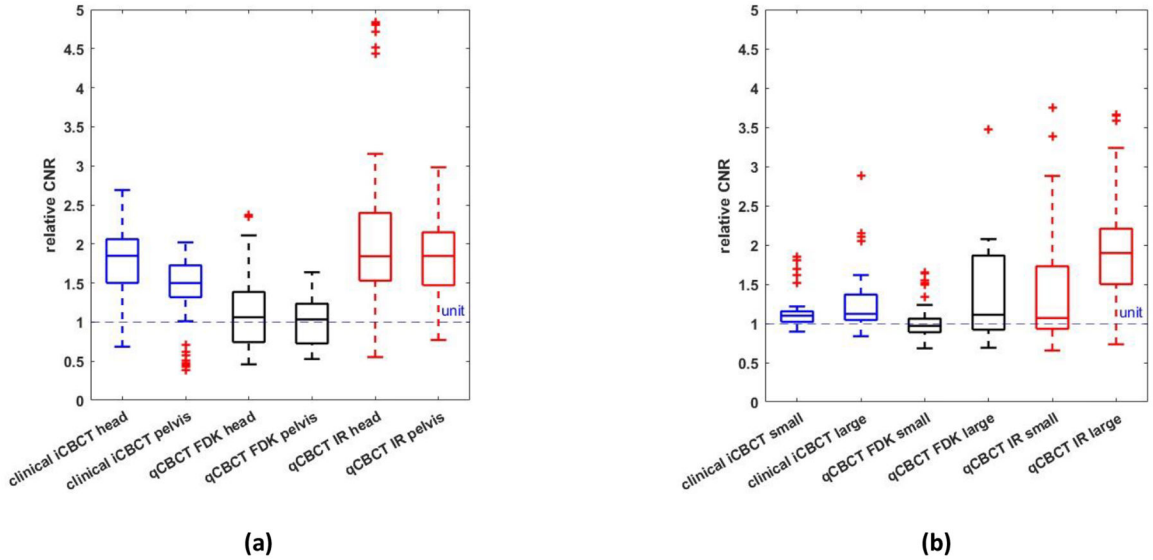

Fig.11.

rCNR as a function of CBCT imaging methods in (a) head and pelvis-sized electron density phantom and (b) small and large Catphan phantoms. Relative CNR is the change in CNR with respect to Clinical FDK reconstructions.

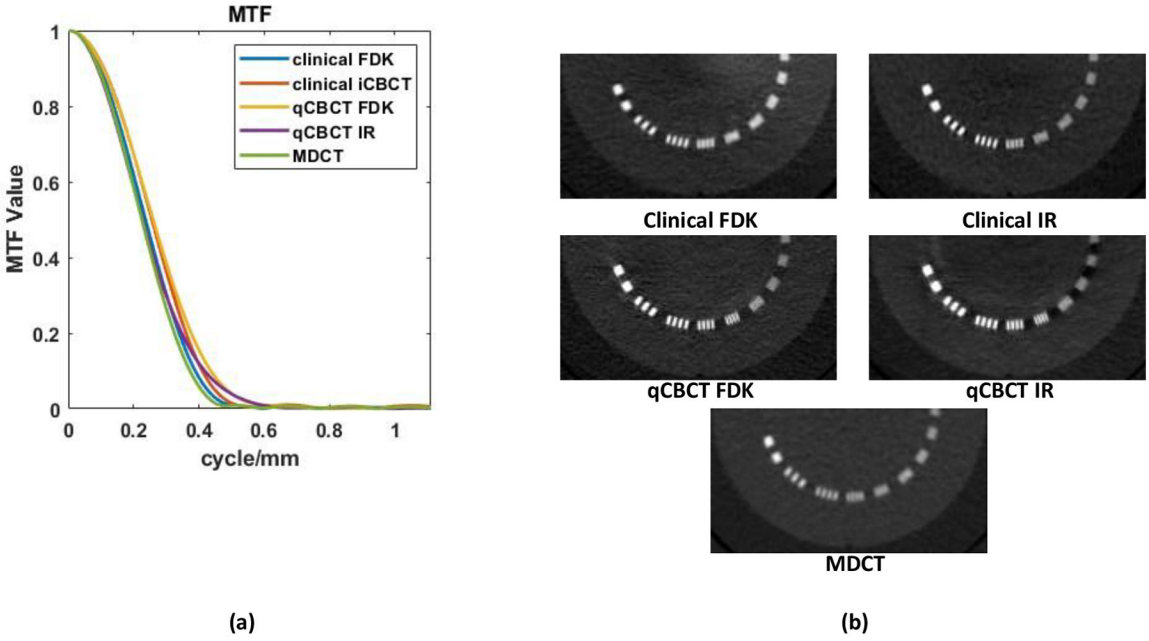

Fig.12.

Comparison of spatial resolution for different imaging methods. (a) MTF and (b) bar pattern phantom images.

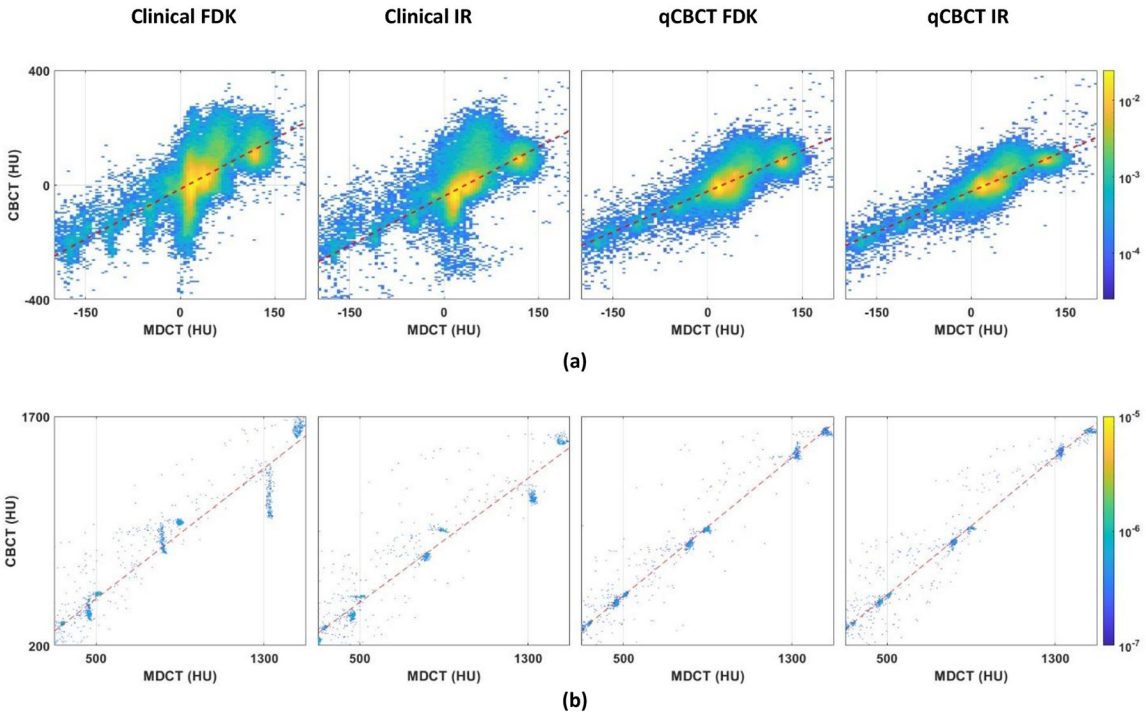

Fig. 13.

Composite HU correlation histograms over all phantoms for each CBCT imaging method. Histograms were generated from (a) soft tissue and (b) bone mimicking regions of each phantom. Expected HU correlation between MDCT and CBCT images is indicated by the dotted line.

Table 1.

HU nonuniformity for all phantoms and imaging methods. Mean ± std.

	Head electron density	Pelvis electron density	Small Catphan	Large Catphan	Thorax	Pelvis	Large pelvis
Clinical FDK	20±14	75±57	6±4	29±21	38±29	18±11	67±31
Clinical IR	13±11	32±20	4±2	19±12	30±19	21±13	49±32
qCBCT FDK	4±4	8±3	6±2	4±4	6±4	14±10	26±18
qCBCT IR	4±4	5±3	2±1	4±3	6±4	14±10	31±20
MDCT	8±4	4±3	0.4±0.5	2±1	3±2	9±7	17±12
p value qCBCT vs MDCT	0.02(*)	0.35 (NS)	0.97 (NS)	1e−2 (*)	8e−3 (*)	0.03 (*)	0.53 (NS)
p value Clinical CBCT vs MDCT	0.04 (*)	5e−6 (*)	5e−3 (*)	3e−5(*)	6e−7(*)	2e−4(*)	1e−3 (*)

Table 2.

Mean and standard deviation of absolute errors in soft tissue mimicking regions of CBCT images when compared to gold standard MDCT images.

	Head electron density	Pelvis electron density	Small Catphan	Large Catphan	Thorax
Clinical FDK	12±10	36±34	8±5	19±14	36±31
Clinical IR	8±8	24±18	6±3	13±9	31±24
qCBCT FDK	9±8	21±16	10±8	18±14	15±13
qCBCT IR	7±7	13±11	8±7	10±8	12±11
p value Clinical IR vs qCBCT IR	0.38	0.02	0.73	0.37	9e-4

Table 3.

Mean and standard deviation of absolute errors in bone mimicking regions of CBCT images when compared to gold standard MDCT images.

	Head electron density	Pelvis electron density	Small Catphan	Large Catphan	Thorax
Clinical FDK	9±8	105±85	73±58	59±28	67±52
Clinical IR	9±6	81±57	65±54	44±32	46±48
qCBCT FDK	7±5	20±15	35±16	28±17	23±22
qCBCT IR	5±4	12±10	34±19	21±15	22±19
p value Clinical IR vs qCBCT IR	0.22	7e−19	0.04	9e−4	7e−6